The Meteoritical Society

Meteoritics & Planetary Science 1–10 (2016)
doi: 10.1111/maps.12655

Exposure and analysis of microparticles embedded in silica aerogel keystones using NF_3-mediated electron beam–induced etching and energy-dispersive X-ray spectroscopy

Aiden A. MARTIN[1], Ting LIN[2], Milos TOTH[1], Andrew J. WESTPHAL[3], Edward P. VICENZI[4], Jeffrey BEEMAN[5], and Eric H. SILVER[2*]

[1]School of Physics and Advanced Materials, University of Technology, Sydney, 15 Broadway, Ultimo, New South Wales 2007, Australia
[2]Harvard-Smithsonian Center for Astrophysics, 60 Garden Street, Cambridge, Massachusetts 02138, USA
[3]Space Sciences Laboratory, University of California at Berkeley, Berkeley, California 94720, USA
[4]Smithsonian Institution, Museum Conservation Institute, 4210 Silver Hill Road, Suitland, California 20746, USA
[5]Materials Sciences Division, Lawrence Berkeley National Laboratory, Berkeley, California 94720, USA
[*]Corresponding author. E-mail: esilver@cfa.harvard.edu

(Received 30 June 2015; revision accepted 17 March 2016)

Abstract–In 2006, NASA's Stardust spacecraft delivered to Earth dust particles collected from the coma of comet 81P/Wild 2, with the goal of furthering the understanding of solar system formation. Stardust cometary samples were collected in a low-density, nanoporous silica aerogel making their study technically challenging. This article demonstrates the identification, exposure, and elemental composition analysis of particles analogous to those collected by NASA's Stardust mission using in-situ SEM techniques. Backscattered electron imaging is shown by experimental observation and Monte Carlo simulation to be suitable for locating particles of a range of sizes relevant to Stardust (down to submicron diameters) embedded within silica aerogel. Selective removal of the silica aerogel encapsulating an embedded particle is performed by cryogenic NF_3-mediated electron beam–induced etching. The porous, low-density nature of the aerogel results in an enhanced etch rate compared with solid material, making it an effective, nonmechanical method for the exposure of particles. After exposure, elemental composition of the particle was analyzed by energy-dispersive X-ray spectroscopy using a high spectral resolution microcalorimeter. Signals from fluorine contamination are shown to correspond to nonremoved silica aerogel and only in residual concentrations.

INTRODUCTION

Studying cometary material is critical for determining the origin and evolution of the solar system. Comets formed from presolar and early nebular matter at the outermost edges of the solar system (Brownlee et al. 2006) and are an archive of chemical and physical processes which occurred during the early evolution of planetary bodies (McKeegan et al. 2006). In 2006, NASA's Stardust spacecraft delivered to Earth thousands of dust particles collected from the coma of comet 81P/Wild 2 for laboratory study (Brownlee et al. 2006). These samples were the first opportunity to directly study cometary particles of known origin in the laboratory (Zolensky et al. 2006). Unlike previous studies of interplanetary dust particles of unknown origin that were collected in Earth's stratosphere, Stardust samples were collected from 81P/Wild 2, which had minimal exposure to the inner solar system, and were collected almost immediately after release from the comet's nucleus. The Stardust dust particles were, therefore, likely shielded from damage by thermal, aqueous, or radiative processes, therefore retaining their properties since early solar system formation (Stodolna et al. 2009).

A portion of the Stardust samples has been analyzed to determine their isotopic (McKeegan et al.

2006), elemental (Keller et al. 2006; Joswiak et al. 2012), structural (Wopenka 2011), and organic (Sandford et al. 2006) composition and complemented by mineralogical and metrological studies using a broad range of techniques, including Raman spectroscopy (Rotundi et al. 2008; Wopenka 2011), infrared spectroscopy (Keller et al. 2006; Matrajt et al. 2008; Rotundi et al. 2008), time-of-flight secondary ion mass spectrometry (Simon et al. 2008; Stephan et al. 2008a, 2008b), nano secondary ion mass spectrometry (Matrajt et al. 2008; Heck et al. 2012), energy-dispersive X-ray spectroscopy (Bridges et al. 2006; Graham et al. 2006; Leroux et al. 2008a; Simon et al. 2008; Stodolna et al. 2009; Heck et al. 2012; Joswiak et al. 2012) (EDS), transmission electron microscopy (Brownlee et al. 2006; Leroux et al. 2008a; Matrajt et al. 2008; Stodolna et al. 2009; Joswiak et al. 2012), electron energy loss spectroscopy (Matrajt et al. 2008; Simon et al. 2008), synchrotron X-ray diffraction (Zolensky et al. 2006), X-ray fluorescence spectroscopy (Matrajt et al. 2008), and X-ray absorption near edge structure spectroscopy (XANES) (Matrajt et al. 2008). Preliminary examinations revealed many surprises, such as a large mineralogical diversity (Joswiak et al. 2012), almost complete absence of water or evidence of aqueous alteration (Keller et al. 2006; Joswiak et al. 2012), and the presence of a calcium–aluminum-rich inclusion and other varieties of presumably high-temperature grains (Nakamura et al. 2008; Simon et al. 2008). These findings have already had major implications for solar nebula models, namely that there appears to be a very efficient mechanism for delivering high-temperature materials to the outer solar system region where comets accreted (Keller et al. 2006; McKeegan et al. 2006; Ciesla 2007).

Stardust cometary samples were collected in a low-density, nano-porous silica aerogel (Tsou 1995). Cometary impact particles are fine-grained and fragile, so generally disintegrate on impact with the aerogel. The largest and most robust particles penetrate deep into the aerogel, but the smallest fragments are distributed nonuniformly along the lengths of carrot-shaped impact tracks (Kearsley et al. 2012). Prior to analysis of the particle, removal from the collection medium is generally required. A process using borosilicate glass microneedles enables the preparation of a silica aerogel keystone containing a complete impact event (Westphal et al. 2004). The process is monitored optically and requires >50,000 discrete automatized motions over many hours to extract the particle from the aerogel. The keystone can then be analyzed or further processed by flattening, mounting on micro-forks, and/or sectioning. Particles and fragments as small as 1 μm across can be extracted by sectioning a keystone embedded in epoxy by ultramicrotomy (Matrajt and Brownlee 2006). Techniques for extracting sub-1 μm particles and fragments are, however, risky. Furthermore, directly observing the removal of small particles is not possible with light-based techniques. Direct nanoscale etching techniques are ideal for this application, and a variety of analytical methods can also be incorporated into these systems for rapid, in-situ analysis of the particles.

In this article, we combine three in-situ scanning electron microscope (SEM) techniques to enable (i) identification, (ii) rapid exposure, and (iii) elemental composition analysis of microparticles embedded in a silica aerogel keystone. A flattened keystone embedded with magnetite and ballistic glass particles was used to replicate Stardust sample conditions. Backscattered electron (BSE) imaging is used to identify particles embedded in silica aerogel. Monte Carlo simulation of electron trajectories in silica aerogel shows that BSE imaging is capable of detecting the embedded particles below the optical detection threshold, with a 100 nm diameter pyrrhotite particle detected at depths up to ~8 μm from the substrate surface. Exposure is performed by cryogenic NF_3-mediated electron beam–induced etching (EBIE) (Utke et al. 2012; Martin and Toth 2014), which gives rise to selective nanoscale chemical etching in areas exposed to an electron beam and enables real-time imaging during etching. Imaging is performed in variable pressure (Danilatos 1988) SEM mode to suppress charging of the electrically insulating silica aerogel (Kucheyev et al. 2007). Finally, the exposed particles are analyzed in-situ by EDS to determine their elemental composition as well as the extent of contamination caused by exposure to NF_3.

MATERIALS AND METHODS

Experiments were performed using an FEI XL30 variable pressure SEM configured for cryogenic NF_3-mediated EBIE and high spectral resolution EDS. The capabilities available on this system enable in-situ identification, exposure, and elemental characterization of particles embedded in silica aerogel keystones (Fig. 1).

Detection of Particles by BSE Imaging

Prior to exposure, the precise location of the particle must be determined in the SEM. Particles are encapsulated by the silica aerogel; therefore, the imaging technique must be capable of generating contrast based on subsurface information. Particles can be identified by light-based or synchrotron X-ray microprobe techniques; however, these require the

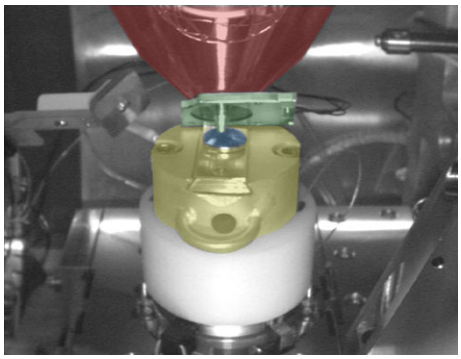

Fig. 1. FEI XL30 SEM configured for cryogenic EBIE, showing the SEM pole piece (highlight in red), BSE detector (green), sample mounting area (blue), and liquid nitrogen cooling stage (yellow).

establishment of a predefined coordinate system and additional handling. Imaging of embedded particles in the SEM using conventional secondary electron detectors is not viable due to the very short escape range of secondary electrons (Reimer 1998). However, BSEs can potentially produce a viable imaging signal (Reimer 1998). Here, we determine the imaging capabilities of BSE imaging via experimental observation and Monte Carlo simulation of electron trajectory in solids (CASINO) program (Demers et al. 2011).

To determine the capability of BSE imaging of detecting embedded particles, a series of images of a piece of silica aerogel covering an aggregate of silver particles was collected using a solid-state BSE detector at varying primary electron energies. Subsurface features are detected by comparing the contrast in the series of images. As the electron accelerating voltage is increased, the penetration range of the electron beam is increased, and an increase in contrast is observed where subsurface features are located. Imaging is performed under a He or NF_3 gaseous environment to suppress electrical charge build-up on the insulating silica aerogel surface. Imaging is performed in He while searching for and after extraction of particles. After locating a particle, the silica aerogel is removed by cryogenic NF_3-mediated EBIE to show the underlying silver aggregate structure for comparison to the subsurface structure revealed by BSE imaging through the silica aerogel. NF_3 is used during etching as the imaging environment to provide real-time information on the removal of aerogel material.

Experiments demonstrate the ability of detecting subsurface particles. However, determining the theoretical detection range of BSE imaging efficiently is difficult. CASINO (software version 3.2.0.4) is used to determine the maximum depth at which BSE imaging can resolve particles embedded in a silica aerogel medium. A pyrrhotite particle ($Fe_{0.83}S$, density: 4.61 g cm^{-3}) of varying size was used as the test particle, with simulations performed at varying primary electron energies and depths of the particle from the surface of nonflattened silica aerogel (SiO_2, density 0.02 g cm^{-3}). Simulations were also performed with diamond (C, density: 3.515 g cm^{-3}) and amorphous silica (SiO_2, density 2.196 g cm^{-3}) particles to determine the capability of BSE imaging of detecting subsurface particles composed of low atomic number material. Properties of nonflattened aerogel were used for this calculation as the result corresponds to a critical keystone cutting parameter. Simulations reveal that BSE imaging will not resolve the buried particle if the cut surface is too far from the particle. At each data point, 250,000 primary electron trajectories were simulated for a 10 nm electron beam spot located at the center of the pyrrhotite particle in the x and y plane. The BSE coefficient at each point was determined by dividing the total number of >50 eV energy electrons escaping the top plane of the silica aerogel by the total number of electrons used in the simulation. We define the particle as resolvable when the BSE coefficient is greater than the BSE coefficient of silica aerogel material.

Exposure of Particles by EBIE

Here, we demonstrate cryogenic NF_3-mediated EBIE (Martin and Toth 2014) (Fig. 2) to be an efficient method to expose particles embedded in silica aerogel. EBIE is a dry, selective chemical etch process where surface adsorbed precursor molecules (i.e., NF_3) are dissociated by an electron beam, producing fragments (F*) that react with surface atoms (Si) to form a volatile compound (SiF_x, where $x = 1 - 4$) that desorbs from the surface, leaving a void. The technique is analogous to Ga^+ focused ion beam (FIB) milling; however, EBIE does not give rise to sputtering, redeposition, and gallium ion implantation (Bassim et al. 2014), which can result in noticeable damage to the particle (Graham et al. 2004).

To ensure that the physical composition of particles is not changed during the exposure process, it is imperative that the EBIE precursor does not react spontaneously. XeF_2, widely used as an EBIE precursor for silicon, is, therefore, not ideal for this application (Winters and Coburn 1992). Here, we have selected NF_3 as the EBIE precursor due to its broad material compatibility (Miotto et al. 2000) and preferential removal of SiO_2 in comparison to other silicon-containing compounds (Martin and Toth 2014). Additionally, when used in a variable pressure electron microscope, qualitative results indicate that NF_3 is an

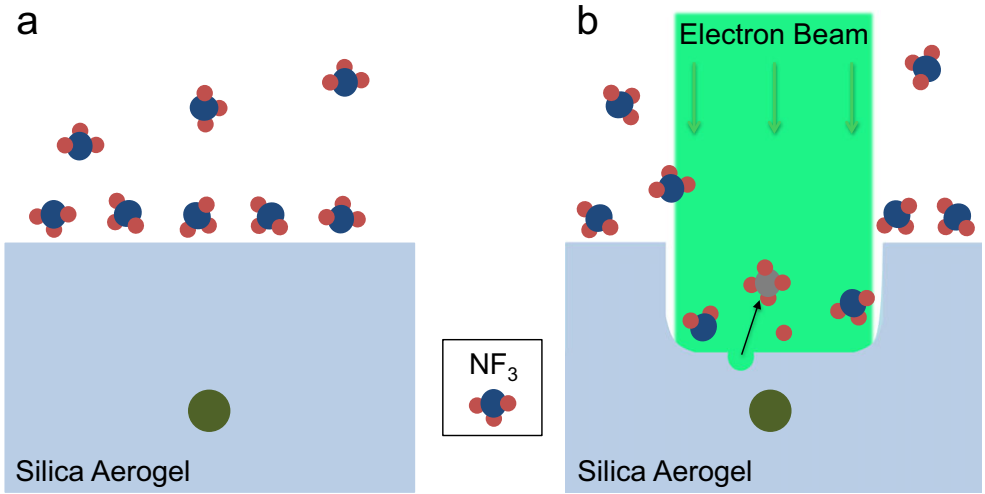

Fig. 2. NF_3-mediated electron beam–induced etching overview. a) NF_3 molecules adsorb to the silica aerogel. b) On exposure to an electron beam, NF_3 molecules dissociate into fragments (F*) that react with the silica aerogel (SiO_2) producing volatile compounds (SiF_x), which desorb from the surface leaving a void.

excellent electronic charge stabilizer during etching and imaging of insulating materials (Martin and Toth 2014), which reduces the probability of particle loss by coulombic repulsion during etching.

A flattened silica aerogel keystone tile embedded with magnetite and ballistic glass particles was used to replicate a returned Stardust cometary sample. Preparation of the Stardust replica sample was performed by Andrew Westphal at the NASA Ames Research Center two-stage light-gas gun facility (Hörz et al. 1998). First, particles of interest are identified by BSE imaging in a He gaseous environment. Cryogenic NF_3-mediated EBIE is then performed by filling the SEM chamber with ~30 Pa of NF_3 and cooling the keystone tile to ~100 K using a liquid nitrogen cold stage. The area of silica aerogel to be removed is scanned by the electron beam in imaging mode to induce etching while observing the etching progress in real time. Etching is halted by blanking the electron beam when complete removal of the silica aerogel surrounding the particle is observed.

Analysis of Particles by X-ray Spectroscopy

After exposure from the silica aerogel keystone, ideally the particle is analyzed prior to exposure to atmosphere. Here, we determine the elemental composition of the particle in-situ by EDS, using a high spectral resolution cryogenic microcalorimeter (Silver et al. 1998) as the X-ray detector (Fig. 3). The microcalorimeter consists of a tin absorber cooled to ~60 mK, doped germanium semiconductor temperature probe, pulse counting unit, and X-ray focusing optic (Silver et al. 2000). X-ray energy is determined by measuring the temperature rise of the tin as it absorbs the incoming X-ray photon. In comparison to conventional silicon drift detectors, the microcalorimeter has superior energy resolution (3 eV instead of 130 eV

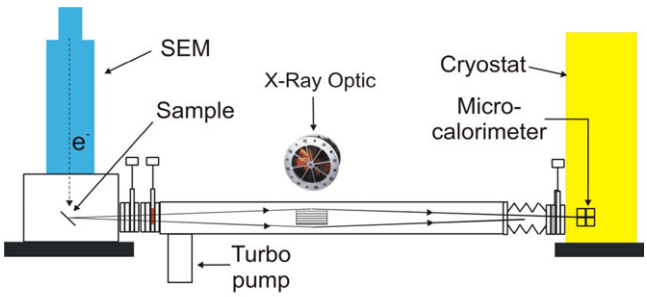

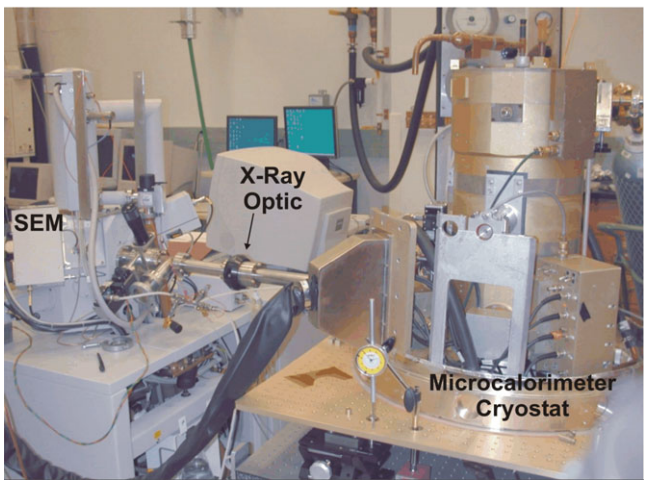

Fig. 3. Schematic of the SEM configured with a high spectral resolution cryogenic microcalorimeter for EDS.

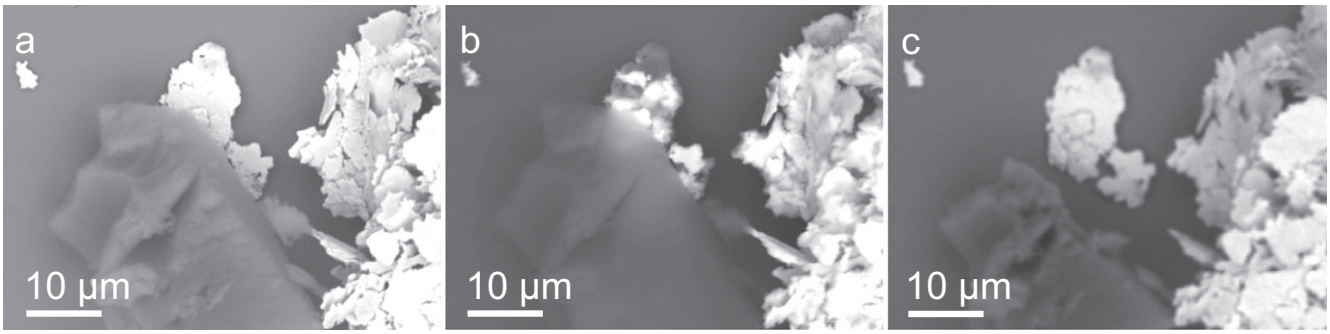

Fig. 4. BSE images of a piece of silica aerogel covering an aggregate of silver particles collected using a (a) 10 and (b) 30 keV primary electron beam. Subsurface objects are revealed by an increase in signal at higher energies. c) Underlying silver aggregate revealed by cryogenic NF_3-mediated EBIE.

at 6 keV X-ray energy) (Silver et al. 2005), providing improved element discrimination. Emitted X-rays are focused by the X-ray optic onto the microcalorimeter detector array significantly increasing the collection solid angle of the detector. In addition, by positioning the X-ray optic focal point at the sample, counts from stray X-rays generated in the gaseous environment of the SEM chamber are minimized.

During the analysis of the exposed particle, NF_3 is removed from the chamber to prevent further etching. EDS is performed under an inert He environment to minimize sample charging and X-rays are excited by a 10 or 15 keV electron beam. Information for the elemental composition maps is collected by rastering an electron beam over the area of interest while simultaneously detecting X-ray photon emission. Elemental composition maps are constructed by plotting the intensity of the X-ray energy of interest as a function of position. Elemental concentration is calculated using the atomic number, absorbance, and fluorescence (ZAF) correction scheme with standards (Scott and Love 1992; Goldstein et al. 2003).

RESULTS AND DISCUSSION

Detection of Particles by BSE Imaging

BSE images of a piece of silica aerogel covering an aggregate of silver particles were collected using a primary electron beam energy of 10 and 30 keV (Fig. 4). At 30 keV, a noticeable increase in signal is observed in the silica aerogel area directly adjacent to the uncovered silver aggregate. To confirm this is a result of subsurface features, the silica aerogel covering the area was removed by cryogenic NF_3-mediated EBIE using the 30 keV electron beam. Figure 4c shows that the silver aggregate did extend under the silica aerogel in the area identified by the BSE image. While silver provides a favorable test case for particle identification due to its high atomic number, this is a positive qualitative result for the identification of embedded particles with BSE imaging.

To quantify the ability of the backscattered imaging technique for detecting embedded particles, simulations using CASINO were performed. Figure 5a shows the BSE coefficient of silica aerogel with an embedded 500 nm diameter pyrrhotite particle as a function of particle depth at 5, 10, 15, and 30 keV primary electron energy. Initially, at shallow depths, the BSE coefficient at all energies is high. As the depth of the particle is increased, the coefficient decreases to a nonzero value corresponding to the BSE coefficient of silica aerogel. While the BSE coefficient at 30 keV is low at shallow depths compared with 10 and 15 keV, the decrease with depth is less pronounced and shows contrast between the measured BSE coefficient and the nonzero background to a depth of ~20 μm. This result shows that higher energies are preferable for detecting particles in initial searches and lower energies are preferable for imaging.

Next, the BSE coefficient as a function of depth at 30 keV primary electron energy was simulated for 100, 200, 500, 1000, and 3000 nm diameter pyrrhotite particles to determine the effect of size on particle detectability (Fig. 5b). The depth at which particles are resolvable is shown to be size dependent, for example, 100, 500, and 3000 nm particles were resolved to a depth of ~8, ~20, and ~60 μm, respectively. The BSE coefficient as a function of depth at 30 keV primary electron energy was also simulated for 500 nm diameter diamond and amorphous silica particles to determine the detectability of low atomic number particles (Fig. 5c). The low atomic number, 500 nm diamond, and amorphous silica particles are resolved to a depth of ~12 μm compared with ~20 μm for the high-density, high atomic number pyrrhotite particle. These simulation results show BSE imaging to be a promising technique for detecting particles in the low-density silica

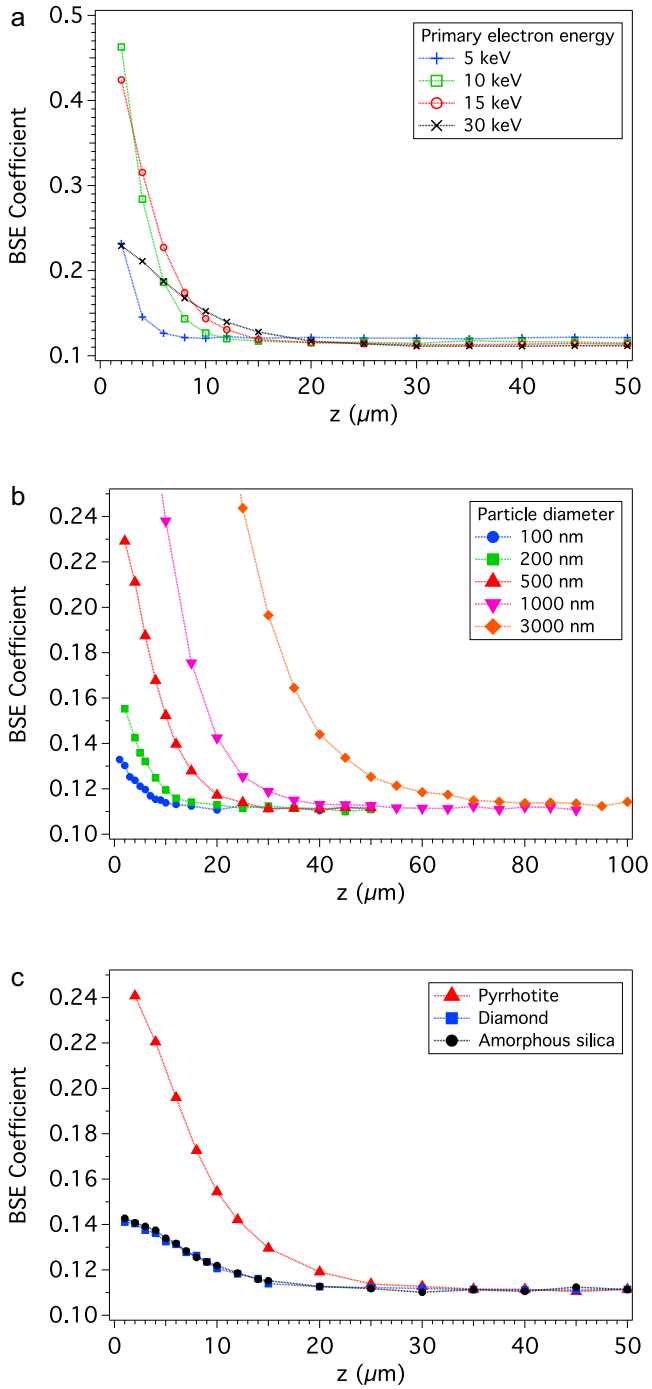

Fig. 5. a) Simulated BSE coefficient of silica aerogel with an embedded 500 nm diameter, spherical pyrrhotite particle as a function of particle depth (z) at 5, 10, 15, and 30 keV primary electron energy. b) Simulated BSE coefficient of silica aerogel with embedded 100, 200, 500, 1000, and 3000 nm diameter pyrrhotite particles as a function of z at 30 keV primary electron energy. c) Simulated BSE coefficient of silica aerogel with an embedded 500 nm diameter pyrrhotite, diamond, and amorphous silica particle as a function of z at 30 keV primary electron energy.

aerogel medium, especially for particles below the resolvable limit of light-based techniques.

Exposure of Particles by EBIE

Cryogenic NF_3-mediated EBIE was performed on the keystone Stardust replica to demonstrate the exposure of an embedded particle (Fig. 6). An area rich in embedded particles was identified by BSE imaging in a He environment using a 30 keV, ~1 nA electron beam. The chamber was then filled with NF_3 and an area containing a large particle of interest imaged by the electron beam for a total of 30 min to induce EBIE, removing the encapsulating silica aerogel. From the size of the particle exposed by EBIE, we estimate that the etch pit depth is of the order of microns in the 79 × 55 μm irradiated area.

The observed volumetric etch rate of material is very high when compared with etching of thermal silicon dioxide material (Martin and Toth 2014). The etch pit depth after 30 min of EBIE in thermal silicon oxide was calculated using a previously reported etch rate under similar conditions (Martin and Toth 2014) (1.1×10^6 nm^3 s^{-1}). The calculated etch pit depth in thermal oxide is only 0.5 nm when processing an area of 79 × 55 μm. The high etch rate in aerogel material arises from the low density and high surface area to volume ratio. The aerogel's high etch rate protects the particle from overexposure to possible EBIE reactions, which could result in removal of material. EBIE processing is, therefore, ideal for removing large volumes of aerogel encapsulating embedded particles. Based on the observed etch rate of silica aerogel material, the exposure of a 3 μm diameter particle by removing a 10 × 10 μm area of surrounding aerogel material would take less than 1 minute.

Analysis of Particles by X-ray Spectroscopy

The exposed particle was analyzed in-situ by EDS to determine its elemental composition and the extent, if any, of fluorine contamination from the EBIE process. EDS was performed using a 10 keV electron beam under a He gaseous environment. False color images of the X-ray intensity assigned to C, Mg, O, Si, Ti, Al, Fe, F, and P as a function of location are shown in Fig. 7. The particle is primarily composed of Si, Mg, and O, with concentrated amounts of Al and a small fraction of Ti. The elemental composition of the particle differs from that expected in ballistic glass (Pyrex, Soda-lime, and Silica-Alumina composites), with no significant abundance of Ca, Na, Al, and/or B present. The composition indicates the particle is a silicate and likely

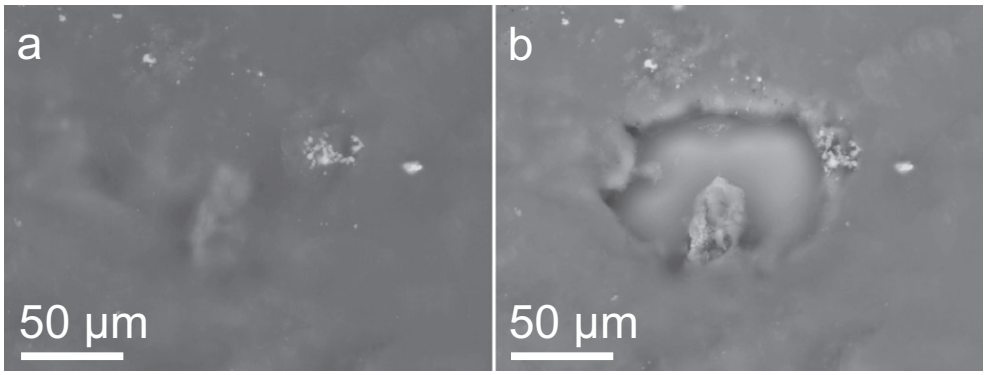

Fig. 6. a) BSE image of a particle embedded in a silica aerogel keystone. b) Removal of encapsulating silica aerogel using cryogenic NF_3-mediated EBIE.

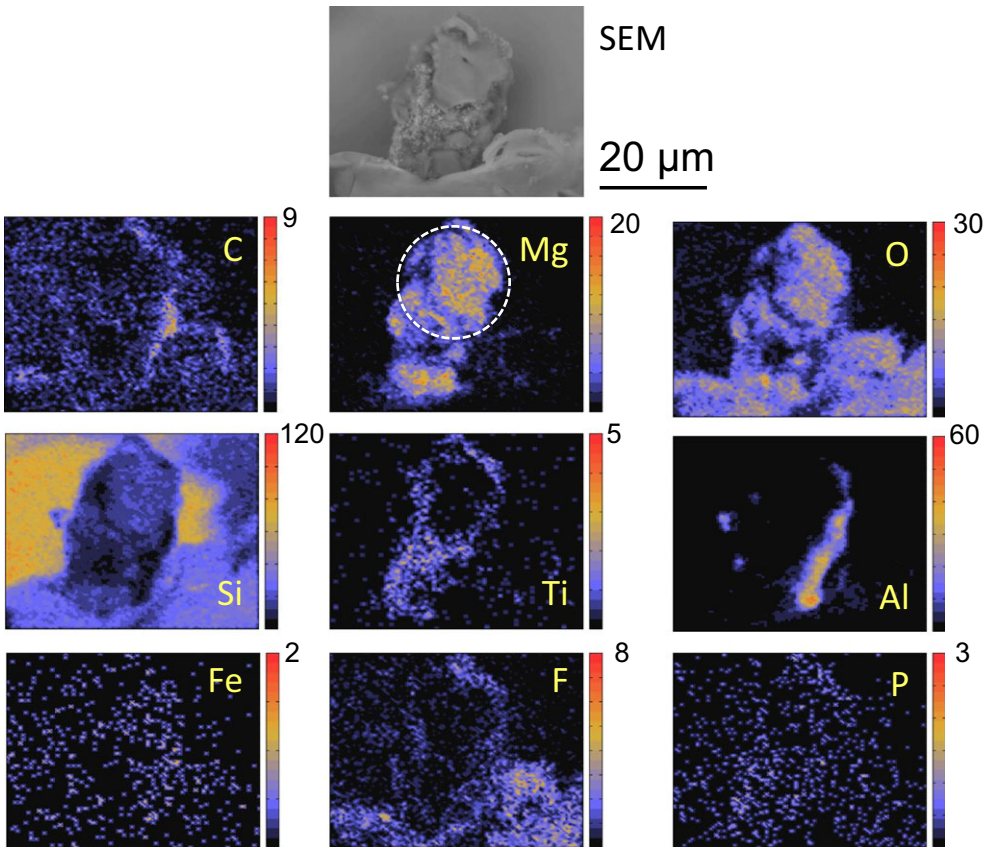

Fig. 7. SEM image and elemental abundance maps of a particle exposed by EBIE. Elemental abundance maps obtained by EDS.

entered the light-gas gun as contamination from previous shots. Importantly, the intensity of detected F is low, and the majority of the signal correlates with areas of nonremoved silica aerogel material.

Figure 8 shows an X-ray spectrum collected from the area circled in Fig. 7 using a 15 keV electron beam under a He gaseous environment. Closer analysis of the particle reveals a small component of residual fluorine, with a concentration of ~0.14%. We ascribe the presence of fluorine to surface functionalization of the particle induced by electron-stimulated desorption of surface species and reaction with NF_3 (Shanley et al. 2014). This may have been exacerbated by overetching in an effort to completely remove any trace of silica aerogel from the particle. Contamination within the aerogel such as Ca, Mg, and Al (Tsou et al. 2003) could also contribute to the detection of fluorine through the production of nonvolatile fluorine compounds

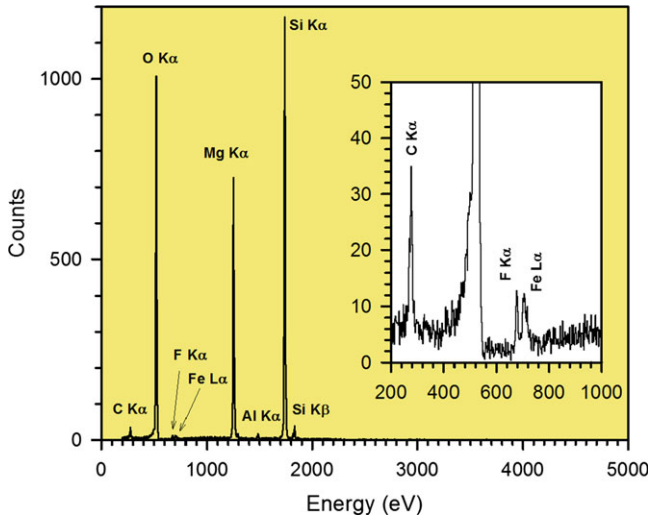

Fig. 8. EDS spectrum of a particle exposed by EBIE (collection area circled in the Mg element map of Fig. 7). The particle is rich in O, Mg, and Si with small traces of F. The F signal intensity corresponds to a concentration of 0.14%, which we ascribe to surface functionalization of the particle with fluorine or formation of nonvolatile fluorine compounds with contaminants present in the silica aerogel.

(e.g., CaF_2, MgF_2, and AlF_3) that remain after EBIE. Interestingly, a signal corresponding to the presence of nitrogen is noticeably absent from our X-ray spectrum. Whether nitrogen is desorbed preferentially by further electron irradiation or simply not adsorbed to the surface is not understood.

CONCLUSIONS

We have demonstrated the identification, rapid exposure, and elemental composition analysis of microparticles embedded in silica aerogel keystones by in-situ SEM-based techniques. BSE imaging is shown by CASINO simulation to detect particles that are below the optical detection limit. The depth at which particles can be resolved is a function of atomic number, particle size, and primary electron energy. After locating an embedded particle, cryogenic NF_3-mediated EBIE successfully removed the encapsulating silica aerogel medium, without physically handling, modifying, or damaging them. EBIE can be applied selectively to many particles within a single impact track. Analysis by EDS using a cryogenic microcalorimeter shows fluorine contamination to be minimal and corresponds to nonremoved silica aerogel. In-situ EDS analysis using a high spectral resolution cryogenic microcalorimeter provides unambiguous detection of light and heavy elements without requiring further processing or exposing the particles to atmosphere.

The combination of these three in-situ techniques provides an excellent platform for the study of Stardust cometary samples, and when optimized, characterizing interstellar cosmic dust particles (Landgraf et al. 1999; Westphal et al. 2014). EBIE can be extended to aerogels of other composition if future missions use these as the collection medium. With the optimization of existing gas precursor chemistries, EBIE could also replace FIB milling for the site-specific exposure of particles preserved in the metal foils found on the outer layers of spacecraft, including Stardust's silica aerogel collector assembly (Bridges et al. 2006; Graham et al. 2006; Leroux et al. 2008b).

Acknowledgments—This work was partly funded by NASA Grant NNX11AF61Gno1 and FEI Company. A.A.M. is the recipient of a John Stocker Postgraduate Scholarship from the Science and Industry Endowment Fund.

Editorial Handling—Dr. Donald Brownlee

REFERENCES

Bassim N., Scott K., and Giannuzzi L. A. 2014. Recent advances in focused ion beam technology and applications. *MRS Bulletin* 39:317–325.

Bridges J. C., Franchi I. A., and Green S. F. 2006. Extraction and analysis of microcrater residues using focused ion beam microscopy (abstract #1664). 37th Lunar and Planetary Science Conference. CD-ROM.

Brownlee D., Tsou P., Aléon J., Alexander C. M. O., Araki T., Bajt S., Baratta G. A., Bastien R., Bland P., Bleuet P., Borg J., Bradley J. P., Brearley A., Brenker F., Brennan S., Bridges J. C., Browning N. D., Brucato J. R., Bullock E., Burchell M. J., Busemann H., Butterworth A., Chaussidon M., Cheuvront A., Chi M., Cintala M. J., Clark B. C., Clemett S. J., Cody G., Colangeli L., Cooper G., Cordier P., Daghlian C., Dai Z., D'Hendecourt L., Djouadi Z., Dominguez G., Duxbury T., Dworkin J. P., Ebel D. S., Economou T. E., Fakra S., Fairey S. A. J., Fallon S., Ferrini G., Ferroir T., Fleckenstein H., Floss C., Flynn G., Franchi I. A., Fries M., Gainsforth Z., Gallien J.-P., Genge M., Gilles M. K., Gillet P., Gilmour J., Glavin D. P., Gounelle M., Grady M. M., Graham G. A., Grant P. G., Green S. F., Grossemy F., Grossman L., Grossman J. N., Guan Y., Hagiya K., Harvey R., Heck P., Herzog G. F., Hoppe P., Hörz F., Huth J., Hutcheon I. D., Ignatyev K., Ishii H., Ito M., Jacob D., Jacobsen C., Jacobsen S., Jones S., Joswiak D., Jurewicz A., Kearsley A. T., Keller L. P., Khodja H., Kilcoyne A. D., Kissel J., Krot A., Langenhorst F., Lanzirotti A., Le L., Leshin L. A., Leitner J., Lemelle L., Leroux H., Liu M.-C., Luening K., Lyon I., MacPherson G., Marcus M. A., Marhas K., Marty B., Matrajt G., McKeegan K., Meibom A., Mennella V., Messenger K., Messenger S., Mikouchi T., Mostefaoui S., Nakamura T., Nakano T., Newville M., Nittler L. R., Ohnishi I., Ohsumi K., Okudaira K., Papanastassiou D. A., Palma R., Palumbo M. E., Pepin R. O., Perkins D., Perronnet M., Pianetta P., Rao W.,

Rietmeijer F. J. M., Robert F., Rost D., Rotundi A., Ryan R., Sandford S. A., Schwandt C. S., See T. H., Schlutter D., Sheffield-Parker J., Simionovici A., Simon S., Sitnitsky I., Snead C. J., Spencer M. K., Stadermann F. J., Steele A., Stephan T., Stroud R., Susini J., Sutton S. R., Suzuki Y., Taheri M., Taylor S., Teslich N., Tomeoka K., Tomioka N., Toppani A., Trigo-Rodríguez J. M., Troadec D., Tsuchiyama A., Tuzzolino A. J., Tyliszczak T., Uesugi K., Velbel M., Vellenga J., Vicenzi E., Vincze L., Warren J., Weber I., Weisberg M., Westphal A. J., Wirick S., Wooden D., Wopenka B., Wozniakiewicz P., Wright I., Yabuta H., Yano H., Young E. D., Zare R. N., Zega T., Ziegler K., Zimmerman L., Zinner E., and Zolensky M. 2006. Comet 81P/Wild 2 under a microscope. *Science* 314:1711–1716.

Ciesla F. J. 2007. Outward transport of high-temperature materials around the midplane of the solar nebula. *Science* 318:613–615.

Danilatos G. D. 1988. Foundations of environmental scanning electron microscopy. *Advances in Electronics and Electron Physics* 71:109–250.

Demers H., Poirier-Demers N., Couture A. R., Joly D., Guilmain M., de Jonge N., and Drouin D. 2011. Three-dimensional electron microscopy simulation with the CASINO Monte Carlo software. *Scanning* 33:135–146.

Goldstein J., Newbury D., Joy D., Lyman C., Echlin P., Lifshin E., Sawyer L. C., and Michael J. R. 2003. *Scanning electron microscopy and x-ray microanalysis*, 3rd edn. New York: Springer.

Graham G. A., Grant P. G., Chater R. J., Westphal A. J., Kearsley A. T., Snead C., Domínguez G., Butterworth A. L., McPhail D. S., Bench G., and Bradley J. P. 2004. Investigation of ion beam techniques for the analysis and exposure of particles encapsulated by silica aerogel: Applicability for Stardust. *Meteoritics & Planetary Science* 39:1461–1473.

Graham G. A., Teslich N., Dai Z. R., Bradley J. P., Kearsley A. T., and Hörz F. 2006. Focused ion beam recovery of hypervelocity impact residue in experimental craters on metallic foils. *Meteoritics & Planetary Science* 41:159–165.

Heck P. R., Hoppe P., and Huth J. 2012. Sulfur four isotope NanoSIMS analysis of comet81P/Wild 2 dust in impact craters on aluminum foil C2037N from NASA's Stardust mission. *Meteoritics & Planetary Science* 47:649–659.

Hörz F., Cintala M. J., Zolensky M. E., Bernhard R. B., Davidson W. E., Haynes G., Thomas H. S., Tsou P., and Brownlee D. E. 1998. *Capture of hypervelocity particles with low-density aerogel*. NASA Technical Memorandum. 98-201792. Houston, Texas: Lyndon B. Johnson Space Center, National Aeronautics and Space Administration.

Joswiak D. J., Brownlee D. E., Matrajt G., Westphal A. J., Snead C. J., and Gainsforth Z. 2012. Comprehensive examination of large mineral and rock fragments in Stardust tracks: Mineralogy, analogous extraterrestrial materials, and source regions. *Meteoritics & Planetary Science* 47:471–524.

Kearsley A. T., Burchell M. J., Price M. C., Cole M. J., Wozniakiewicz P. J., Ishii H. A., Bradley J. P., Fries M., and Foster N. J. 2012. Experimental impact features in Stardust aerogel: How track morphology reflects particle structure, composition, and density. *Meteoritics & Planetary Science* 47:737–762.

Keller L. P., Bajt S., Baratta G. A., Borg J., Bradley J. P., Brownlee D. E., Busemann H., Brucato J. R., Burchell M., Colangeli L., d'Hendecourt L., Djouadi Z., Ferrini G., Flynn G., Franchi I. A., Fries M., Grady M. M., Graham G. A., Grossemy F., Kearsley A., Matrajt G., Nakamura-Messenger K., Mennella V., Nittler L., Palumbo M. E., Stadermann F. J., Tsou P., Rotundi A., Sandford S. A., Snead C., Steele A., Wooden D., and Zolensky M. 2006. Infrared spectroscopy of comet 81P/Wild 2 samples returned by Stardust. *Science* 314:1728–1731.

Kucheyev S. O., Toth M., Baumann T. F., Hamza A. V., Ilavsky J., Knowles W. R., Saw C. K., Thiel B. L., Tileli V., van Buuren T., Wang Y. M., and Willey T. M. 2007. Structure of low-density nanoporous dielectrics revealed by low-vacuum electron microscopy and small-angle x-ray scattering. *Langmuir* 23:353–356.

Landgraf M., Müller M., and Grün E. 1999. Prediction of the in-situ dust measurements of the stardust mission to comet 81P/Wild 2. *Planetary and Space Science* 47:1029–1050.

Leroux H., Rietmeijer F. J. M., Velbel M. A., Brearley A. J., Jacob D., Langenhorst F., Bridges J. C., Zega T. J., Stroud R. M., Cordier P., Harvey R. P., Lee M., Gounelle M., and Zolensky M. E. 2008a. A TEM study of thermally modified comet 81P/Wild 2 dust particles by interactions with the aerogel matrix during the Stardust capture process. *Meteoritics & Planetary Science* 43:97–120.

Leroux H., Stroud R. M., Dai Z. R., Graham G. A., Troadec D., Bradley J. P., Teslich N., Borg J., Kearsley A. T., and Hörz F. 2008b. Transmission electron microscopy of cometary residues from micron-sized craters in the Stardust Al foils. *Meteoritics & Planetary Science* 43:143–160.

Martin A. A. and Toth M. 2014. Cryogenic electron beam induced chemical etching. *ACS Applied Materials & Interfaces* 6:18,457–18,460.

Matrajt G. and Brownlee D. E. 2006. Acrylic embedding of Stardust particles encased in aerogel. *Meteoritics & Planetary Science* 41:1715–1720.

Matrajt G., Ito M., Wirick S., Messenger S., Brownlee D. E., Joswiak D., Flynn G., Sandford S., Snead C., and Westphal A. 2008. Carbon investigation of two Stardust particles: A TEM, NanoSIMS, and XANES study. *Meteoritics & Planetary Science* 43:315–334.

McKeegan K. D., Aléon J., Bradley J., Brownlee D., Busemann H., Butterworth A., Chaussidon M., Fallon S., Floss C., Gilmour J., Gounelle M., Graham G., Guan Y., Heck P. R., Hoppe P., Hutcheon I. D., Huth J., Ishii H., Ito M., Jacobsen S. B., Kearsley A., Leshin L. A., Liu M.-C., Lyon I., Marhas K., Marty B., Matrajt G., Meibom A., Messenger S., Mostefaoui S., Mukhopadhyay S., Nakamura-Messenger K., Nittler L., Palma R., Pepin R. O., Papanastassiou D. A., Robert F., Schlutter D., Snead C. J., Stadermann F. J., Stroud R., Tsou P., Westphal A., Young E. D., Ziegler K., Zimmermann L., and Zinner E. 2006. Isotopic compositions of cometary matter returned by Stardust. *Science* 314:1724–1728.

Miotto R., Ferraz A., and Srivastava G. 2000. Dissociative adsorption of NF_3 on Si(001)-(2x1). *Surface Science* 454–456:152–156.

Nakamura T., Noguchi T., Tsuchiyama A., Ushikubo T., Kita N. T., Valley J. W., Zolensky M. E., Kakazu Y., Sakamoto K., Mashio E., Uesugi K., and Nakano T.

2008. Chondrulelike objects in short-period comet 81P/Wild 2. *Science* 321:1664–1667.

Reimer L. 1998. *Scanning electron microscopy: Physics of image formation and microanalysis*. Paris: Springer Verlag.

Rotundi A., Baratta G. A., Borg J., Brucato J. R., Busemann H., Colangeli L., D'Hendecourt L., Djouadi Z., Ferrini G., Franchi I. A., Fries M., Grossemy F., Keller L. P., Mennella V., Nakamura K., Nittler L. R., Palumbo M. E., Sandford S. A., Steele A., and Wopenka B. 2008. Combined micro-Raman, micro-infrared, and field emission scanning electron microscope analyses of comet 81P/Wild 2 particles collected by Stardust. *Meteoritics & Planetary Science* 43:367–397.

Sandford S. A., Aléon J., Alexander C. M. O., Araki T., Bajt S., Baratta G. A., Borg J., Bradley J. P., Brownlee D. E., Brucato J. R., Burchell M. J., Busemann H., Butterworth A., Clemett S. J., Cody G., Colangeli L., Cooper G., D'Hendecourt L., Djouadi Z., Dworkin J. P., Ferrini G., Fleckenstein H., Flynn G. J., Franchi I. A., Fries M., Gilles M. K., Glavin D. P., Gounelle M., Grossemy F., Jacobsen C., Keller L. P., Kilcoyne A. L. D., Leitner J., Matrajt G., Meibom A., Mennella V., Mostefaoui S., Nittler L. R., Palumbo M. E., Papanastassiou D. A., Robert F., Rotundi A., Snead C. J., Spencer M. K., Stadermann F. J., Steele A., Stephan T., Tsou P., Tyliszczak T., Westphal A. J., Wirick S., Wopenka B., Yabuta H., Zare R. N., and Zolensky M. E. 2006. Organics captured from comet 81P/Wild 2 by the Stardust spacecraft. *Science* 314:1720–1724.

Scott V. D. and Love G. 1992. Formulation of a universal electron probe microanalysis correction method. *X-Ray Spectrometry* 21:27–35.

Shanley T. W., Martin A. A., Aharonovich I., and Toth M. 2014. Localized chemical switching of the charge state of nitrogen-vacancy luminescence centers in diamond. *Applied Physics Letters* 105:063103.

Silver E. H., Legros M., Madden N. W., Goulding F., and Landis D. 1998. *Broadband high resolution X-ray spectral analyzer*. US Patent 5777336. Washington, D.C.: United States Patent and Trademark Office.

Silver E. H., Schnopper H. W., and Ingram R. 2000. *X-ray diagnostic system*. US Patent 6094471. Washington, D.C.: United States Patent and Trademark Office.

Silver E., Beeman J., Goulding F., Haller E. E., Landis D., and Madden N. 2005. A NTD germanium-based microcalorimeter with 3.1 eV energy resolution at 6 keV. *Nuclear Instruments and Methods in Physics Research* 545:683–689.

Simon S. B., Joswiak D. J., Ishii H. A., Bradley J. P., Chi M., Grossman L., Aléon J., Brownlee D. E., Fallon S., Hutcheon I. D., Matrajt G., and Mckeegan K. D. 2008. A refractory inclusion returned by Stardust from comet 81P/Wild 2. *Meteoritics & Planetary Science* 43:1861–1877.

Stephan T., Rost D., Vicenzi E. P., Bullock E. S., MacPherson G. J., Westphal A. J., Snead C. J., Flynn G. J., Sandford S. A., and Zolensky M. E. 2008a. TOF-SIMS analysis of cometary matter in stardust aerogel tracks. *Meteoritics & Planetary Science* 43:233–246.

Stephan T., Flynn G. J., Sandford S. A., and Zolensky M. E. 2008b. TOF-SIMS analysis of cometary particles extracted from Stardust aerogel. *Meteoritics & Planetary Science* 43:285–298.

Stodolna J., Jacob D., and Leroux H. 2009. A TEM study of four particles extracted from the Stardust track 80. *Meteoritics & Planetary Science* 44:1511–1518.

Tsou P. 1995. Silica aerogel captures cosmic dust intact. *Journal of Non-Crystalline Solids* 186:415–427.

Tsou P., Brownlee D. E., Sandford S. A., Hörz F., and Zolensky M. E. 2003. Wild 2 and interstellar sample collection and Earth return. *Journal of Geophysical Research: Planets* 108:8113.

Utke I., Moshkalev S., and Russell P. 2012. *Nanofabrication using focused ion and electron beams: Principles and applications*. New York: Oxford University Press.

Westphal A. J., Snead C., Butterworth A., Graham G. A., Bradley J. P., Bajt S., Grant P. G., Bench G., Brennan S., and Pianetta P. 2004. Aerogel keystones: Extraction of complete hypervelocity impact events from aerogel collectors. *Meteoritics & Planetary Science* 39:1375–1386.

Westphal A. J., Stroud R. M., Bechtel H. A., Brenker F. E., Butterworth A. L., Flynn G. J., Frank D. R., Gainsforth Z., Hillier J. K., Postberg F., Simionovici A. S., Sterken V. J., Nittler L. R., Allen C., Anderson D., Ansari A., Bajt S., Bastien R. K., Bassim N., Bridges J., Brownlee D. E., Burchell M., Burghammer M., Changela H., Cloetens P., Davis A. M., Doll R., Floss C., Grün E., Heck P. R., Hoppe P., Hudson B., Huth J., Kearsley A., King A. J., Lai B., Leitner J., Lemelle L., Leonard A., Leroux H., Lettieri R., Marchant W., Ogliore R., Ong W. J., Price M. C., Sandford S. A., Tresseras J.-A. S., Schmitz S., Schoonjans T., Schreiber K., Silversmit G., Solé V. A., Srama R., Stadermann F., Stephan T., Stodolna J., Sutton S., Trieloff M., Tsou P., Tyliszczak T., Vekemans B., Vincze L., Von Korff J., Wordsworth N., Zevin D., and Zolensky M. E., and 30714 Stardust@home dusters. 2014. Evidence for interstellar origin of seven dust particles collected by the Stardust spacecraft. *Science* 345:786–791.

Winters H. F. and Coburn J. W. 1992. Surface science aspects of etching reactions. *Surface Science Reports* 14:161–269.

Wopenka B. 2011. Raman spectroscopic investigation of two grains from comet 81P/Wild 2: Information that can be obtained beyond the presence of sp^2-bonded carbon. *Meteoritics & Planetary Science* 47:565–584.

Zolensky M. E., Zega T. J., Yano H., Wirick S., Westphal A. J., Weisberg M. K., Weber I., Warren J. L., Velbel M. A., Tsuchiyama A., Tsou P., Toppani A., Tomioka N., Tomeoka K., Teslich N., Taheri M., Susini J., Stroud R., Stephan T., Stadermann F. J., Snead C. J., Simon S. B., Simionovici A., See T. H., Robert F., Rietmeijer F. J. M., Rao W., Perronnet M. C., Papanastassiou D. A., Okudaira K., Ohsumi K., Ohnishi I., Nakamura-Messenger K., Nakamura T., Mostefaoui S., Mikouchi T., Meibom A., Matrajt G., Marcus M. A., Leroux H., Lemelle L., Le L., Lanzirotti A., Langenhorst F., Krot A. N., Keller L. P., Kearsley A. T., Joswiak D., Jacob D., Ishii H., Harvey R., Hagiya K., Grossman L., Grossman J. N., Graham G. A., Gounelle M., Gillet P., Genge M. J., Flynn G., Ferroir T., Fallon S., Ebel D. S., Dai Z. R., Cordier P., Clark B., Chi M., Butterworth A. L., Brownlee D. E., Bridges J. C., Brennan S., Brearley A., Bradley J. P., Bleuet P., Bland P. A., and Bastien R. 2006. Mineralogy and petrology of comet 81P/Wild 2 nucleus samples. *Science* 314:1735–1739.